

Contents lists available at ScienceDirect

Micron

journal homepage: www.elsevier.com/locate/micron



Check for updates

Spatial resolution in transmission electron microscopy

R.F. Egerton^{a,*}, M. Watanabe^b

- a Physics Department, University of Alberta, Edmonton T6G 2E1, Canada
- b Department of Materials Science and Engineering, Lehigh University, Bethlehem, PA 18015, USA

ARTICLE INFO

Keywords: Resolution Image contrast Point-spread function TEM STEM

ABSTRACT

We review the practical factors that determine the spatial resolution of transmission electron microscopy (TEM) and scanning-transmission electron microscopy (STEM), then enumerate the advantages of representing resolution in terms of a point-spread function. PSFs are given for the major resolution-limiting factors: aperture diffraction, spherical and chromatic aberration, beam divergence, beam broadening, Coulomb delocalization, radiolysis damage and secondary-electron generation from adatoms or atoms in a matrix. We note various definitions of beam broadening, complications of describing this effect in very thin specimens, and ways of optimizing the resolution in bright-field STEM of thick samples. Beam spreading in amorphous and crystalline materials is compared by means of simulations. For beam-sensitive specimens, we emphasize the importance of dose-limited resolution (DLR) and briefly recognize efforts to overcome the fundamental resolution limits set by the wave and particle properties of electrons.

1. Introduction

Resolution is a central goal in microscopy, whether carried out using electrons, photons or some other particle. It can be specified in a variety of ways but the emphasis here will be on the use of a point-spread function (PSF) to describe not only instrumental performance but also the behavior of electrons within a thin TEM sample. Together with doselimited resolution (DLR), these point-spread functions determine the image quality that is achievable in electron microscopy.

Electrons have the big advantage that their deBroglie wavelength λ is less than 10 pm (0.1 Å) if they are accelerated through a potential difference of at least 20 keV. The wavelength limit to resolution Δx , given by the Rayleigh criterion:

$$\Delta x \sim 0.6 \lambda / \sin \alpha$$
 (1)

then has subatomic dimensions, provided the TEM or STEM objective lens can focus electrons traveling up to an angle α of around 10 mrad (about 0.6 degrees) relative to the optic axis. Glass lenses focus light over a much larger angular range but electron lenses have aberrations that are both larger and more difficult to correct. When properly aligned, magnetic hexapoles and octupoles can correct spherical aberration up to typically 30 mrad and provide a resolution of the order of 100 pm (e.g. Haider et al., 2008). This subatomic resolution allows small displacements of atoms to be measured and the atomic structure of defects (such

The above summary ignores the practical difficulties involved and the diverse possibilities of analytical TEM. For a more realistic discussion, we need to address some of the limiting factors that contribute to image resolution, as summarized in Table 1.

2. Practical aspects

Before a high-resolution TEM is installed, its location has to be carefully considered, since the potential resolution can be destroyed by several kinds of interference. STEM images are particularly sensitive to fluctuations in magnetic field, which should be below 0.2 mG (peak-to-peak) for 0.2 nm resolution (Muller and Grazul, 2001). In fact, less than 0.1 mG is preferred nowadays, especially in the vertical direction. Aside from transformers, electric motors and the like, a common source of stray field is a "ground loop" in the electrical wiring, when the neutral wire has been connected to ground *locally* so that the neutral- and live-wire currents do not balance. Magnetic interference from pumps and power supplies is reduced by locating these items in a separate room. If the magnetic field cannot be reduced sufficiently, a TEM can be shielded by mu-metal sheets or the field compensated by large Helmholz coils, driven by the amplified signal from a magnetic-field sensor, although these solutions tend to be expensive and not always completely

E-mail address: regerton@ualberta.ca (R.F. Egerton).

as dislocations or grain boundaries) to be studied; see for example Warner et al. (2012), Lee and Han (2021).

^{*} Corresponding author.

Table 1Factors affecting the spatial resolution of TEM measurements. The first three represent engineering challenges, the last three relate to physical limits.

limitation: contributing factors:
environment vibration, B-field, P & T changes
electronics drift, ripple, readout rate
electron optics apertures, lens aberrations, alignment
beam spreading elastic scattering, specimen thickness
Coulomb delocalization inelastic scattering, energy loss eV
electron statistics drift, radiation damage, collection efficiency

effective.

Electron energy-loss spectrometers are also sensitive to magnetic fields, which degrade the *energy* resolution. Camera chambers that have a glass window (and may be made from brass) cause the spectrometer to be sensitive to ac fields and to movement of metal objects such as chairs.

Mechanical vibration also destroys spatial resolution. Active vibration mounts are available but a less expensive solution is to install the TEM on a concrete block or horizontal slab (Turner et al., 1997). Even so, it is challenging to deal with very low vibration frequencies (below 10 Hz).

Temperature changes around the TEM column cause an expansion or contraction that is seen as specimen drift. Side-entry stages are particularly prone to this problem. Besides temperature stabilization of the lens-cooling water, a common policy nowadays is to ensure low airflow in the TEM room and install water-cooled panels on the internal walls. Another recent trend is to enclose the TEM in a metal box, protecting the column from air currents.

Pressure changes (due to doors opening *etc.*) can influence a sideentry stage and are minimized by placing an enclosure around the specimen-exchange area. Sound vibrations are attenuated by soundabsorbing panels. Noise problems, as well as pressure and temperature changes, are reduced if the TEM is located in a room separate from the microscope control desk.

TEM resolution is compromised by any instability in the electronics, such as drift and ripple in the lens and high-voltage power supplies. Although the highest accelerating voltage gives the shortest electron wavelength, it has not provided the best resolution due to the difficulty of stabilizing voltages of the order of 1 MV. Power-supply stability has improved over the years but optimum performance requires hand-picked components, making the equipment expensive. This situation has improved recently due to the use of high-brightness electron sources and the increased speed of readout electronics: if an image or spectrum

can be acquired in a shorter time, electrical and mechanical drift become less important.

2.1. Electron optics

TEM resolution obviously depends on the quality of the electron optics, including lens design, machining accuracy of the lens polepieces and the magnetic uniformity of polepiece materials. Axial astigmatism, a defect in first-order focusing, is corrected by incorporating an objective-lens stigmator (a pair of weak quadrupoles). Problems associated with lens aberrations are minimized by accurate alignment of the optical components (lenses and apertures) and more recently by incorporating an aberration corrector, which itself requires very accurate alignment (Batson, 2009). Spherical-aberration correctors work only up to a certain angular limit (equivalent to a resolution of typically 25λ) and actually increase the amount of higher-order aberration above that limit

The resolution also depends on which TEM imaging mode is employed. For example, bright-field *diffraction* contrast is easy to use but its resolution is limited by diffraction at an *objective aperture*, which must be small in order to select a limited angular range.

Assuming perfect alignment and zero astigmatism but no aberration correction, the resolution of a TEM or STEM is determined mainly by *spherical* aberration, which introduces an image-plane blurring (but referred to specimen-plane dimensions) given by:

$$\Delta r_{\rm s} = C_{\rm s} \alpha^3 \tag{2}$$

 C_s is the spherical-aberration coefficient of the objective lens, roughly equal to its focal length f, and α is the divergence semi-angle of electrons leaving the specimen (for TEM) or probe-convergence semi-angle (for STEM), approximately equal to R/f where R is the radius of the objective aperture. A small aperture decreases Δr_s but increases the aperture-diffraction broadening Δx , given by Eq. (1). The overall blurring Δr due to both effects is often estimated by adding the individual broadenings in quadrature:

$$(\Delta r)^2 = (\Delta r_s)^2 + (\Delta x)^2 \tag{3}$$

Plotted against α , Δr has a minimum value that represents an optimum resolution. However, this simple treatment hides some important details that are revealed by representing the aberration and diffraction effects in terms of response functions, rather than single numbers.

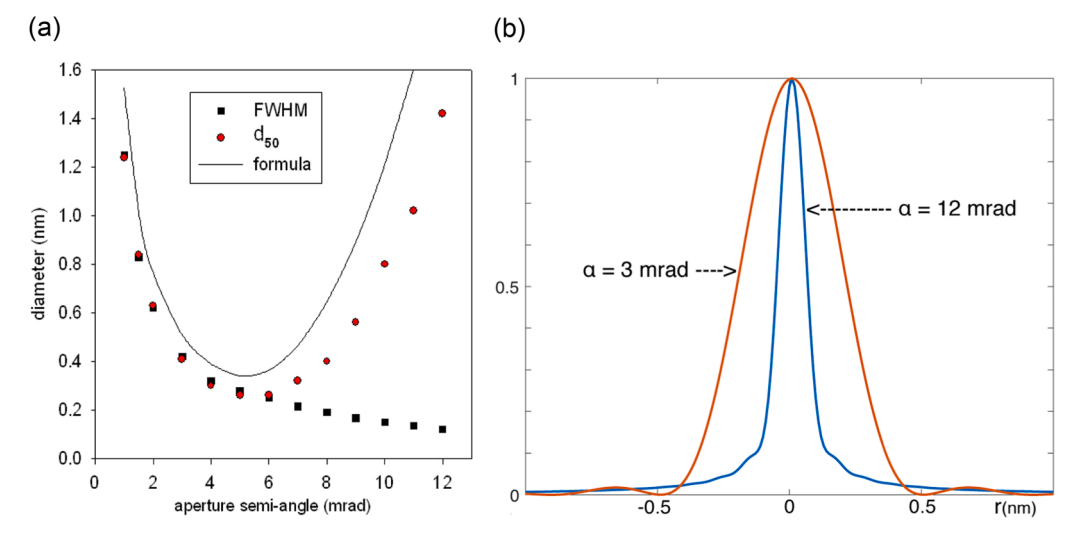


Fig. 1. (a) Combined effect of spherical aberration and aperture diffraction, represented by a smooth curve derived from Eq. (3), and also by the FWHM (square data points) and diameter d_{50} (circular data points) derived from Eq. (7). (b) Point-spread functions for two values of the objective-lens semi-angle α, derived from Eq. (7). The simulation assumes $C_s = 1.2$ mm and λ = 25 pm (200 keV electrons).

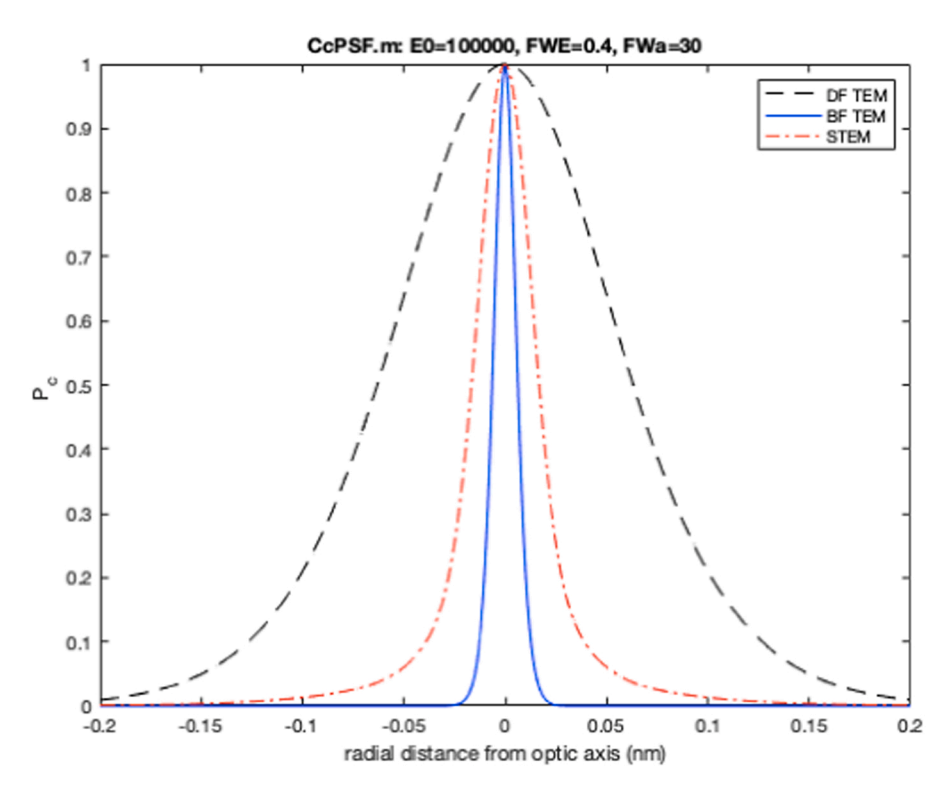


Fig. 2. Chromatic-aberration PSF for scattering-contrast imaging of an organic specimen, in a 100 kV TEM with a 10-mrad objective aperture in dark-field mode (dashed curve) and 1-mad illumination convergence in bright-field mode (solid blue curve). The specimen is assumed to be sufficiently thin that *single* inelastic scattering predominates ($t < \lambda_i$, the inelastic mean free path) and gives an energy width of 40 eV. The dash-dot red curve is for 100 kV STEM imaging with a probe convergence semi-angle of 30 mrad, assuming an incident-probe energy width of 0.4 eV.

3. Point-spread function (PSF)

In electron microscopy, a point-spread function describes the radial distribution of electron flux (intensity) within a disk of confusion that should ideally be a single point. For example, a perfect electron lens would focus a point source of electrons to a single point in the image. In the presence of lens aberrations, this becomes a disk of confusion of radius $M\Delta r_s$ (where M is the image magnification) or just Δr_s when referred to the object plane (as needed for specifying resolution). However, most electrons travel at some smaller angle θ relative to the optic axis, arriving with a radial displacement $C_s\theta$ ³. The intensity dI/dA within the disk of confusion can be calculated if we know the flux per unit solid angle $dI/d\Omega$. The simplest case corresponds to uniform intensity within the angle-limiting aperture ($dI/d\Omega$ = constant), giving an object-plane flux distribution equal to (Egerton and Crozier, 1997):

$$P_{\rm s} = (3\pi C_{\rm s}^{2/3} \alpha^2)^{-1} (1/r^{4/3}) \tag{4}$$

This point-spread function P_s has a singularity at r=0 but is normalized for an r-integral of 1.

Without spherical aberration, a uniformly filled aperture would give an intensity distribution described by an Airy function:

$$P_{\mathbf{a}} = \left[2J_{1}(\rho)/\rho\right]^{2} \tag{5}$$

where $\rho=(2\pi/\lambda)\alpha r$ and J_1 is a first-order Bessel function. Eq. (5) can be viewed as the PSF of the aperture, and $P_{\rm d}=1$ at r=0. Its central peak is close to a Gaussian function:

$$G = \exp[-r^2\alpha^2/(0.31\lambda)^2] \tag{6}$$

with a full width at half maximum (FWHM) equal to $0.51\lambda/\alpha$. This Gaussian approximation is useful for predicting the resolution of fine detail but the Airy function has satellite maxima that together contribute about 16% to the total intensity, generating a long-range background signal that reduces contrast and blurs edge features in the image.

Under appropriate conditions (discussed below), the combined effect of spherical aberration and aperture diffraction is described by a point-spread function given by:

$$P_{\rm sa} = P_{\rm s} \otimes P_{\rm a} \tag{7}$$

where \otimes represents a convolution. In this case, the convolution is two-dimensional, since P_s and P_a are actually two-dimensional functions having radial symmetry about the optic axis.

Fig. 1a shows several measures of image resolution, plotted against objective-aperture size for a typical 200 kV TEM. For small α , aperture diffraction dominates: the FWHM and the diameter d_{50} containing 50% of the electrons, both obtained using Eq. (7), are close to the Δr value given by Eq. (3). As α increases, the FWHM (representing the width of the central peak of $P_{\rm Sa}$) continues to decrease, allowing fine detail of a specimen to remain visible in the image. However, increasing spherical aberration adds extended tails to $P_{\rm Sa}$, as seen from Fig. 1b and from increasing values of the diameter d_{50} containing 50% of the electrons (circular data points in Fig. 1a).

In the case of a repeating structure, such as atoms in a crystalline specimen, the PSF tails from neighboring atoms overlap, reducing the contrast and possibly making the atoms invisible due to the presence of statistical noise. If the atoms are sufficiently far apart, the sharp central peak of the PSF may ensure visibility, which explains why heavy atoms dispersed on a thin carbon film could be imaged with a STEM whose probe diameter was as large as 0.5 nm (Crewe et al., 1970). In general, the central peak of the PSF determines how much fine detail (of high spatial frequency) appears in the image, whereas the PSF tails determine the overall contrast. The Fourier transform of the PSF is a modulation transfer function (MTF).

Geometric optics can also be used to derive a PSF for chromaticaberration broadening:

$$P_{c}(r) \propto \int I(\theta)[J(E)/E^{2}] dE$$
 (8)

where $\theta = E_0 C_c^1 E^1 r$ and $I(\theta)$ represents the number of electrons per unit solid angle (between the objective lens and the specimen) contributing to the image contrast. For TEM imaging, J(E) is the energy-loss spectrum of the specimen, plus a small contribution from energy spread of the illumination, and $I(\theta)$ represents scattering within the objective-aperture angle α (in dark field imaging) and angular divergence of the

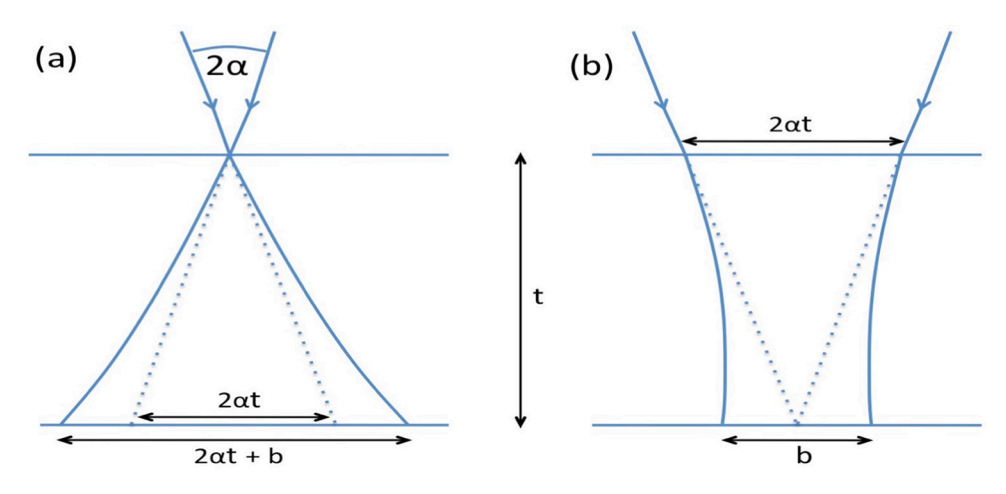


Fig. 3. The spreading effects of beam divergence (dotted lines) combined with beam broadening (solid curves). (a) Electron beam of convergence semi-angle α focused to a point on the beam-entrance surface of a specimen of thickness t, where beam divergence gives an exit-plane diameter $2\alpha t$ and beam broadening increases this geometrical effect by an amount b. (b) Same beam focused on beam-exit surface; beam divergence gives an entrance-surface diameter $2\alpha t$ and an exit-surface diameter b.

illumination (in bright-field imaging). In STEM, $I(\theta)$ and J(E) represent the angular convergence and the energy spread of the incident probe, with no contribution from the specimen since the transmitted electrons are not imaged electron-optically. Fig. 2 shows computed $P_c(r)$ for TEM and STEM imaging of a thin specimen using 100 keV electrons. Chromatic aberration is more troublesome for thick specimens or a TEM operated below 50-kV accelerating voltage, where the energy and angular widths are increased by plural scattering.

In the STEM case, there will also be an image broadening due to the electron-source diameter (appreciable for a thermionic source) whose current-density distribution is that of the source with radial dimensions reduced by the source/specimen demagnification factor. The PSFs given in Eqs. (4)–(8) are for a Gaussian image plane, with paraxial rays precisely in focus. By appropriate defocus, the FWHM of the central peak can be decreased by up to 30% but at the expense of additional intensity in the tails (Kirkland, 2020).

The discussion above has involved electron intensity, without reference to electron phase. This is appropriate for incoherent imaging: the norm in light optics and valid in electron microscopy under certain conditions. These include: incoherent illumination (e.g. from a thermionic electron source), incoherent scattering (e.g. STEM imaging with high-angle dark-field detector), thick or amorphous specimens, and a phase-uncorrelated signal (e.g. x-ray mapping with an energy-dispersive detector). In such cases, simple convolution as in Eq. (7) can be used to combine properties of the imaging system and scattering properties of beam electrons within the specimen. Phase-contrast images represent a different situation: the PSF is complex (having amplitude and phase) and image simulation typically requires computer modeling (e.g. Kirkland, 2020). However, it is interesting to note that Spence (2013, p.62) derived an image-intensity PSF (impulse response) for use with a weak phase object.

4. Beam properties within the specimen

The remaining resolution factors to be discussed relate to the behavior of electrons within the specimen and their arrival at a detector. Any change in diameter of the electron probe will affect the resolution of a STEM image and possibly the spatial resolution of an analytical signal.

For example, if a STEM probe of convergence semi-angle α (but negligible diameter) is focused on the beam-entrance face of a specimen of thickness t, its geometrical diameter $d_{\rm g}$ at the beam-exit surface is (2t) tan $\alpha \sim 2\alpha t$, as shown in Fig. 3a. The exit-plane diameter containing 50% of the electrons is therefore:

$$d_{50} = (2t/2^{1/2}) \tan \alpha \sim 1.4 \ \alpha t \tag{9}$$

If the same probe is focused on beam-exit surface, its beam-entrance diameter is $2\alpha t$; see Fig. 3b. In either case, the irradiated volume of

 $\label{eq:continuous_problem} \textbf{Table 2} \\ \textbf{STEM-image broadening of features (\textit{e.g. particles}) at the beam-entrance or beam-exit surfaces of a sample, for probe focused on either surface: FW = focal width, BD = beam divergence, BB = beam broadening.}$

probe focus at:	particle at:	broadening
entrance	entrance	FW
entrance	exit	FW+BD+BB
exit	entrance	FW+BD
exit	exit	FW+BB

specimen is $(\pi/3) \alpha^2 t^3$, equal to that of a cylinder of diameter 1.15 αt , and x-rays can be emitted from anywhere within this volume as a result of this beam divergence (BD) effect.

If the electron intensity per unit solid angle is uniform within the angle α , the PSF for beam divergence at a distance z from the beam focus is a rectangular (top-hat) function of width $2\alpha z$. The diameter containing 50% of the electrons is then $2^{1/2}\alpha t$ at the exit-plane surface or $0.82\alpha t$ if averaged over the specimen thickness.

As illustrated in Fig. 3, the scattering of electrons further increases the exit-beam diameter by an amount b, an effect known as beam broadening or beam spreading. The cause is almost entirely elastic scattering, since the angles of inelastic scattering are much smaller. Beam broadening is more important in thicker specimens, particularly if they contain elements of high atomic number that give rise to strong elastic scattering.

In reality, a probe focused at the specimen's entrance surface will have a non-zero diameter, due to aperture diffraction and any lens aberrations. This focal width (FW) will affect the beam diameter at all planes within the specimen, whereas the effect of beam divergence and beam broadening vary with depth and position of the focus, as summarized in Table 2. The result of all three effects can be estimated by quadrature addition, as in Eq. (3), but more quantitative treatment would be to convolve the associated point-spread functions.

Beam broadening degrades the best-obtainable STEM resolution at a beam-exit surface, known as a *top-bottom effect* (Gentsch et al., 1974). By depositing small gold particles on both surfaces and recording their STEM-image diameters for a probe focused on each surface, the individual broadening effects can be separated and measured (Hyun et al., 2008).

In general, beam divergence predominates for the large-angle probes that are possible with aberration-corrected optics, whereas beam broadening is more important for specimens containing elements of high atomic number.

In the case of an SEM bulk specimen, beam broadening gives rise to the pear-shaped interaction volume whose width accounts for the roughly 1-micron resolution in SEM x-ray images. This lateral spreading does not affect the SEM secondary-electron image, since secondaries

escape only if they are generated close to the surface where the spread is minimal.

In TEM imaging, the incident-beam divergence is relatively small and the incident-beam diameter does not directly affect the image resolution. However not all planes within the specimen are precisely in focus, leading to a depth-of-field blurring (the equivalent of beam divergence in STEM) that depends on the angular width of the scattering and the objective-aperture diameter. Beam broadening in TEM might be equated with curvature of the electron trajectories due to plural scattering, which also leads to loss of resolution.

4.1. Quantitative measures of beam broadening

As noted by Van Cappellan and Schmitz (1992), several different measures are used to describe beam broadening. It is commonly specified in terms of the percentage x of electrons within a given diameter, x = 50% being often used for qualitative analysis or elemental mapping and x = 90% or 95% for quantitative analysis. For STEM imaging, an exit-plane broadening may be specified or an average broadening (diameter of a cylinder of volume equal to that of the spreading cone) in the case of elemental mapping using emitted x-rays.

Instead of a radial distribution of intensity, some authors compute a y-integrated intensity as a function of the perpendicular x-coordinate (Rez, 1983). This seems equivalent to a line-spread function (LSF), which is slightly broader than the corresponding point-spread function and is appropriate to the analysis of a linear object (such as a grain boundary) rather than a point-like object such as a small precipitate. Yet another definition uses the distance between 25% and 75% intensity points at a step edge (Reimer and Kohl, 2008), or between 12% and 88% (Michael and Williams, 1987). These various definitions yield somewhat different numbers but what is usually required is a reliable estimate rather than an accurate value.

4.2. Beam-broadening models

The simplest and best-known model for beam spreading is that of Goldstein et al. (1977), developed for x-ray analysis in the TEM and intended to give a *thickness-averaged* diameter containing 90% of the electrons:

$$b_{90} = 0.20 F_{\rm r} (Z/E_0) (\rho/A)^{1/2} t^{3/2}$$
(10)

In Eq. (10), b_{90} and the specimen thickness t are expressed in nm, the incident energy E_0 is in keV and $F_r=1$ (non-relativistic approximation). Z and A are the atomic number and atomic weight (mass number) of the specimen, ρ being its density in g/cm^3 . The $t^{3/2}$ thickness dependence arises because the single-scattering intensity (relative to the unscattered beam) is proportional t while the *angular* width of *plural* scattering increases as $t^{1/2}$.

Eq. (10) was obtained by setting the probability $P(>\alpha)$ of elastic scattering through angles greater than α equal to 0.1, this probability being based on the angular distribution of elastic scattering provided by the Rutherford formula for scattering from a bare atomic nucleus. The beam broadening is then taken as $b_{90} = \alpha t$, which would be exact if all scattering took place at the mid-plane of the foil. However, this last assumption can be avoided (within a single-scattering approximation) by integrating over the 90% angular cone, which increases b_{90} by only 15%. Although it neglects atomic screening effects that become important at lower scattering angles, use of the Rutherford formula is justified when α is large and $P(>\alpha)$ small. For high accelerating voltages, Eq. (10) can be made relativistic by setting $F_r = (1 + E_0/511)/(1 + E_0/1022)$ (Reimer and Kohl, 2008), giving $F_r = 1.16$ at $E_0 = 200$ keV.

Cliff and Lorimer (1981) used a Lenz (screened-Rutherford) model

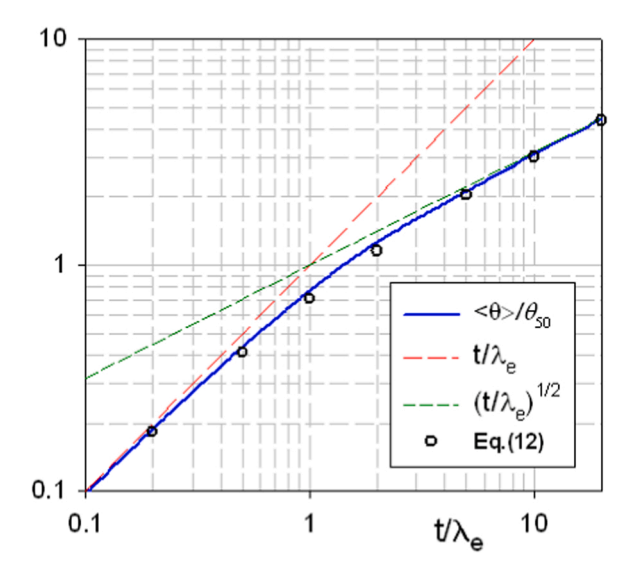


Fig. 4. Blue curve: ratio f(t) of the mean scattering angle $<\theta>$ per primary electron to the median angle θ_{50} of single scattering, plotted as a function of normalized specimen thickness t/λ_e , where λ_e is a mean free path for elastic scattering. Solid circles: approximation to f(t) given by Eq. (12).

for the single-scattering angular distribution but noted that for thick specimens the angular and spatial distributions should become Gaussian (Bothe, 1951), in accordance with the central limit theorem. To their surprise, they found Eq. (10) to be a good approximation for thicker specimens. On the other hand, Gauvin and Rudinski (2016) argue that the broadening should become proportional to t^2 for very thin films: the angular width and probability of *single* scattering are both proportional to t, giving a product proportional to t^2 . They model the transition from single to multiple scattering by writing the broadening as $b = \lambda_e \theta * (t/\lambda_e)^{1+H}$ where λ_e and θ^* are a mean free path and average angle of inelastic scattering, while H is a Hurst exponent derived from fractal considerations (Mandelbrot, 1982): H = 0.5 corresponds to normal diffusion and H = 1 to ballistic behavior.

Here we use Poisson statistics to provide an alternative description of the transition from single to plural scattering and to illustrate some complications of defining beam broadening in very thin specimens. If the median angle of single elastic scattering is θ_{50} , the average angle for n-fold scattering is $\theta_{n} = n^{1/2} \, \theta_{50}$ according to random-walk behavior of the radial displacement. The scattering angle averaged over all primary electrons (including the unscattered beam) is then:

$$\langle \theta \rangle = \exp(-t/\lambda_e) \, \Sigma_n \, (n^{1/2} \theta_{50}) (t/\lambda_e)^n / n! = f(t) \, \theta_{50} \tag{11}$$

where λ_e is the elastic mean free path and n is summed from 0 to ∞ . Numerical evaluation of Eq. (11) gives the continuous blue curve in Fig. 4 and shows that f(t) can be approximated as:

$$f(t) = [(t/\lambda_e)^{-1} + (t/\lambda_e)^{-2}]^{-1/2}$$
(12)

Assuming scattering at the mid-plane, the median radial displacement at the specimen exit plane is $r=(t/2)\langle\theta\rangle$ and the median exit-plane diameter is:

$$b_{50} = t \langle \theta \rangle = t f(t) \theta_{50} \tag{13}$$

For $t/\lambda_{\rm e} <<1$, $b_{50} \propto t^2$ while for $t/\lambda_{\rm e}>>1$, $b_{50} \propto t^{3/2}$, as derived by Gauvin and Rudinski (2016) and consistent with measurements and Monte Carlo calculations (de Jonge et al., 2018; Drees et al., 2018).

Eq. (13) can be generalized to give a diameter b_x containing x percent of the transmitted electrons:

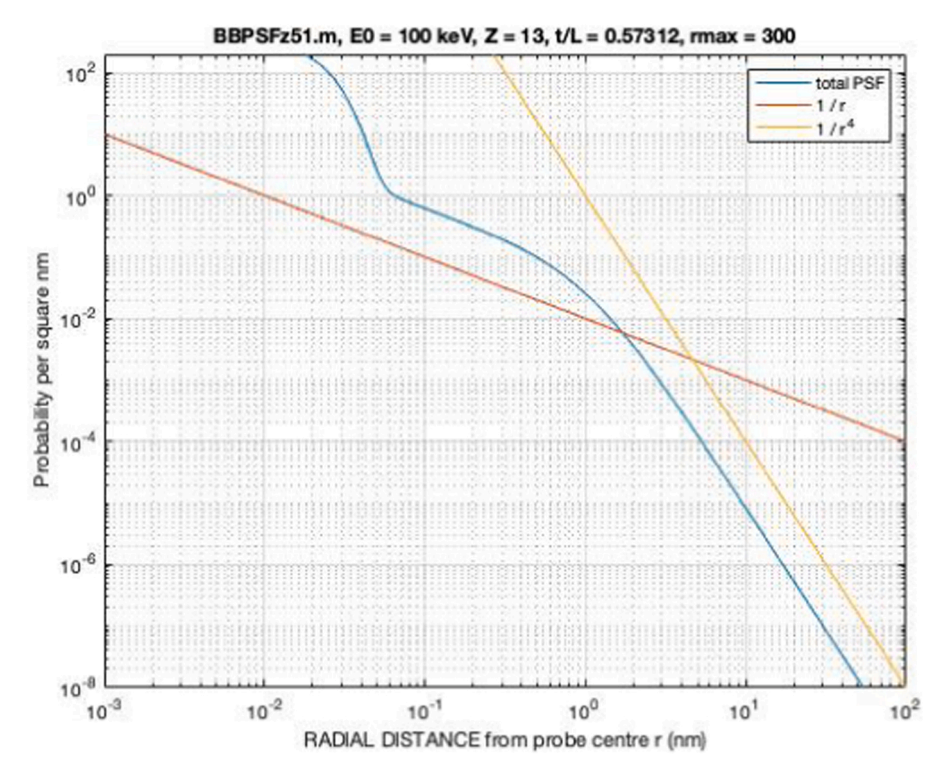


Fig. 5. Blue curve: point-spread function $P_b(r,t)$ for broadening of a 0.1 nm-diameter beam of 100 keV electrons after traveling through a thickness t = 100 nm of aluminum, calculated from Eq. (19) using the Lenz model of elastic scattering and displayed on logarithmic axes. Data for r < 0.05 nm represent the unscattered beam. Red and yellow lines show r^1 and r^4 dependencies.

$$b_{X} = t f(t) \theta_{X} \tag{14}$$

where the average angle θ_x containing x% of the *single-scattered* electrons is given (Gauvin and Rudinsky, 2016), by:

$$\theta_{x} = \left[x/(100-x) \right]^{1/2} \theta_{50} \tag{15}$$

To estimate $b_{\rm x}$ we can use the Lenz atomic model, which gives the median single-scattering angle as:

$$\theta_{50} = \lambda Z^{1/3} / (2\pi a_0) \tag{16}$$

where λ is the primary-electron wavelength and $a_0=52.9$ pm. If the specimen density ρ is expressed in g/cm³, the Lenz value of the elastic mean free path (in nm) is:

$$\lambda_{\rm e} = (890/\rho)(A/Z^{4/3})(v/c)^2 \tag{17}$$

where $(v/c)^2 = E_0(E_0 + 1022)/(E_0 + 511)^2$ with the primary energy E_0 in keV. Values of d_{90} calculated from Eq. (14) are close to those calculated from Eq. (10) for $t > \lambda_e$ but scale proportional to t^2 for small thickness.

In fact, defining x as a percentage of the transmitted (rather than the scattered) electrons becomes problematical for very thin films. According to Poisson statistics, more than x% of electrons remain *unscattered* when $t/\lambda_e < \ln(100/x)$, so for very thin films ($t < 0.7\lambda_e$ for x = 50 or $t < \lambda_e/10$ for x = 90) b_x becomes meaningless as a measure of beam broadening. This problem disappears when we describe beam spreading in terms of its point-spread function.

4.3. Beam-broadening PSF

A more universal and complete description of beam broadening is

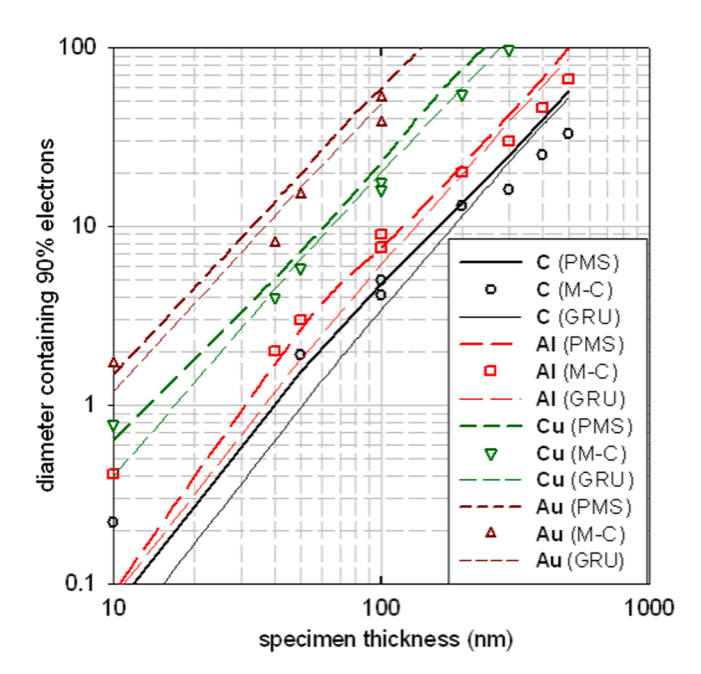


Fig. 6. Thick lines (PMS): exit-surface diameter (in nm) containing 90% of the 100 keV electrons transmitted through specimens of carbon, aluminum, copper and gold, based on Eq. (19) and plotted against specimen thickness. Data points: diameter of a cylinder whose volume contains 90% of the electrons, from Monte Carlo calculations (Newbury and Myklebust, 1979; Kyser, 1979). Thin lines (GRU): 90%-cylinder diameter given by Eq. (14).

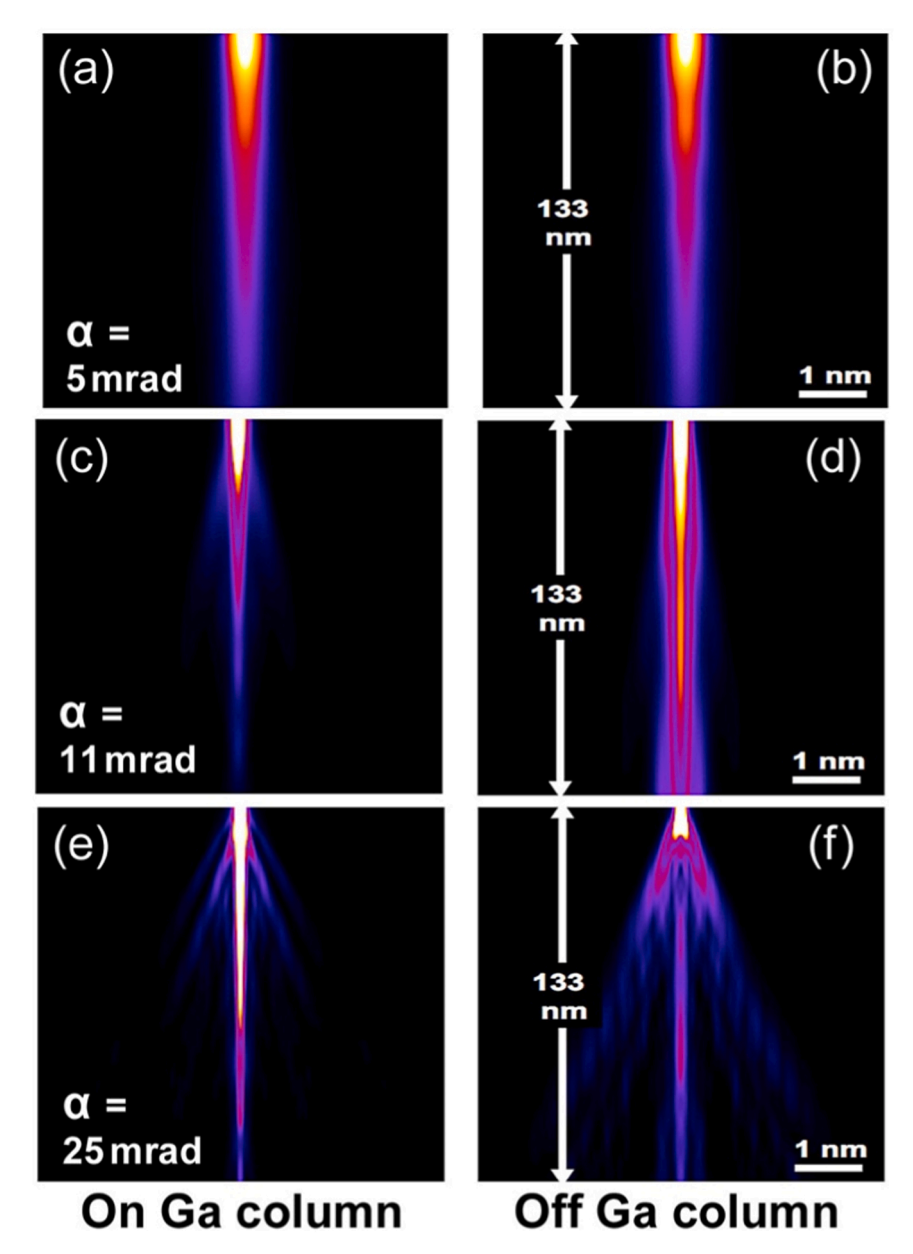


Fig. 7. xHREM simulations of beam spreading in a single-crystal specimen of GaAs, for a small probe of 200 keV electrons focused on the top (beam-entrance) surface and centered (on the left) on Ga atomic columns, and (on the right) between atomic columns.

given by its PSF, based on a model for the intensity and angular distribution of single elastic scattering, together with a realistic treatment of plural scattering throughout the specimen. For the latter, one option is to use the Poisson formula in a differential form: the change dP_n in the probability of n-fold scattering within a slice of thickness dz is:

$$dP_{n} = (1/n!) \varepsilon [n(m)^{n-1} - (m)^{n}] dm$$
(18)

where $m=z/\lambda_e$ and $\varepsilon=\exp(-m)$. The first and second terms within the square brackets represent the increase in n-fold scattering within a slice and the decrease arising from higher-order (n+1) scattering, respectively. Summing over orders of scattering and integrating over slices gives the point-spread function at a depth z below the entrance surface:

$$P_{\rm b}(r,z) = \varepsilon \, \delta(r) + \Sigma_{\rm n} \int \{ S^{\rm n}(r/h) \, \varepsilon \, (n/n!) \, m^{\rm n-1} - [\int S^{\rm n}(r/h) \, \varepsilon \, (n/n!) \, m^{\rm n-1} \, {\rm d}m] \} {\rm d}m$$
(19)

The first term represents the unscattered beam and $S^{n}(r/h)$ is a

normalized angular distribution of n-fold elastic scattering. An example of the numerical evaluation of Eq. (19) is shown by the blue curve in Fig. 5. Red and yellow lines illustrate r^1 and r^4 dependencies at small and large values of the radial distance r, which appear to be consistent with the PSF deduced from Monte Carlo calculations.

Numerical procedures for Monte Carlo calculations are described in numerous publications (e.g. Joy, 1995; Hovington et al., 1997; Geiss and Kyser, 1979; Kyser, 1979; Newbury and Myklebust, 1979). This method can be used for thick specimens, where multiple scattering is predominant (Demers et al., 2012). An atomic model is used to simulate elastic scattering and it is possible to also incorporate inelastic scattering, based on Bethe theory. The main effect of inelastic scattering is to slow down the electrons so that the elastic scattering becomes stronger and more divergent. For TEM samples, the rate of energy loss of a 100 keV electron (in eV/nm, for a specimen of density ρ g/cm³) is: $dE/dz\approx0.3~\rho$, which represents a change in elastic-scattering power of less than 1% for an organic specimen of thickness 1000 nm. Fig. 6 shows published Monte

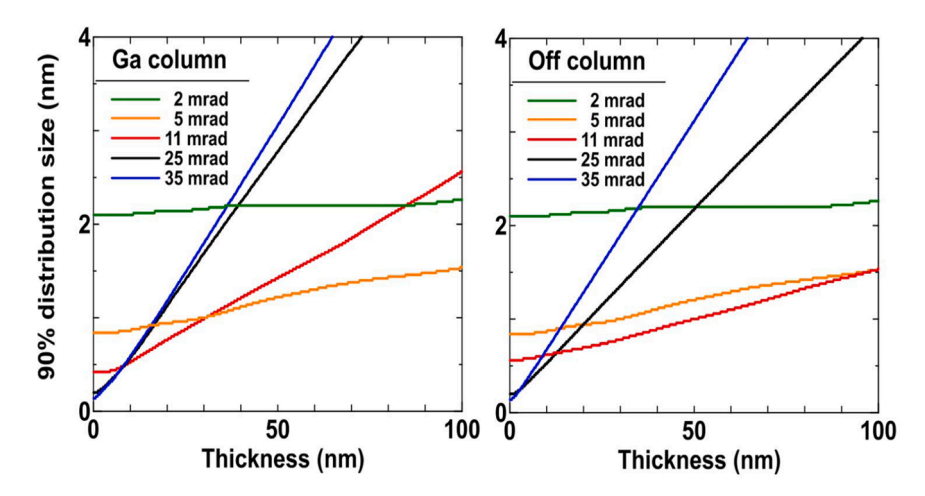


Fig. 8. Diameter d₉₀ containing 90% of the transmitted electrons, calculated for [100] electron propagation in GaAs, assuming an aberration-free objective lens.

Carlo data compared with results obtained from Eq.(14) and from the Poisson-multislice (PMS) method, Eq. (19).

A treatment of beam broadening using the Boltzman transport equation is also possible (Groves, 1975; Rose, 1975). Data for silicon, iron and gold films of thickness between 10 nm and 400 nm are given by Rez (1983) but the method can also be applied to the thick (e.g. 1 μ m) specimens used in tomography (Wolf et al., 2018), where multiple scattering determines the image resolution.

4.4. TEM and STEM imaging of thick specimens

If a *thick* specimen (*e.g.* 1000 nm of biological tissue) is imaged in TEM mode, the resolution is typically limited by chromatic aberration arising from energy loss of the transmitted electrons. An accurate description for different imaging modes might involve calculating the chromatic PSF from Eq. (19), with the energy distribution J(E) obtained by self-convolution of a single-scattering profile. However, a rough estimate of the resolution limit is given by the traditional formula:

$$\Delta r_{\rm c} = C_{\rm c} \; \alpha \; \Delta E/E_0(20)$$

where α is a range of scattering angles imaged by the objective lens (focal length f, chromatic aberration coefficient C_c), which is usually limited by an objective aperture of diameter D to give $2\alpha \sim D/f$. For the energy spread ΔE we can take the mean energy loss *per incident electron*:

$$\langle E \rangle = (t/\lambda_i)E_{av}$$
 (21)

where λ_i is the inelastic mean free path and $E_{\rm av}$ is the mean energy loss per inelastic scattering event, roughly 7Z for atomic number Z < 20 (Egerton, 2021). For an organic sample of thickness t = 1000 nm, Eq. (21) gives $\Delta r_{\rm c}$ 12 nm for $E_0 = 200$ keV but improving to $\Delta r_{\rm c} \sim 0.6$ nm for $E_0 = 2$ MeV if $C_{\rm c} = 1.5$ mm.

Unfortunately, conventional high-voltage TEMs are very large and expensive. Compact 2–3 MeV sources are available that produce pulsed beams with a pulse length as short as 200 fs and energy spread of some tens of eV. The electrons can be focused by quadrupole lens systems that are compact and efficient, with a focal length of typically 15 mm. The resolution of a 5-element quadrupole lens has been calculated to be better than 1 nm for $\alpha=0.7$ mrad and $\Delta E/E_0=10^{-5}$ (Wan et al., 2018). But Coulomb repulsion between the electrons precludes beam-beam diameters below about 30 μm , which is sufficient or ultra-fast electron diffraction (UED) but will not allow high-resolution imaging unless the pulse repetition rate can be increased by a few orders of magnitude above the rate ($\sim 100~{\rm Hz})$ currently available.

Chromatic aberration in STEM mode, which depends on the energy and angular widths of the incident probe, is generally less than for TEM but the beam-divergence broadening d_g (due to the probe convergence

angle α) can be large. Annular dark-field resolution is further degraded by beam broadening but for bright-field imaging its effect can be reduced by placing an aperture in front of the STEM detector and the resulting improvement in resolution has been confirmed by Monte Carlo calculations (Sousa et al., 2009). Rez et al. (2016) calculated this improvement for thick specimens of ice and protein, assuming parallel illumination with 200-keV electrons. For high-resolution STEM the incident-probe divergence will be dominant but for probe and collection semi-angles of the order of 1 mrad, resolution of 2 nm seems possible, with an order-of-magnitude loss of signal due to the reduced collection efficiency.

A more sophisticated control of beam broadening, together with depth resolution, involves a confocal arrangement (Zaluzec, 2003). With aberration correction of both the imaging and probe-forming lenses, three-dimensional imaging with atomic-scale lateral resolution and a depth resolution of a few nm should be possible (Nellist et al., 2006).

For organic specimens, we must also consider radiation damage and the resulting dose-limited resolution, which depends on image contrast (discussed below). Contrast mechanisms in thick organic specimens are discussed by Wolf et al. (2018) and Elbaum et al. (2021).

4.5. Crystalline specimens

The analytical and Monte Carlo models discussed above all use an *atomic* model for the elastic scattering and are only strictly applicable to amorphous specimens. In a polycrystalline or single-crystal specimen, electron diffraction adds a pronounced directionality to the scattering, while channeling effects make this diffraction sensitive to the probe position and specimen orientation.

However, it is possible to model the elastic scattering in a thin crystalline specimen by using a multislice program, such as the xHREM package (Ishizuka, 2012). Operational details of the calculation can be found in the literature (Watanabe and Egerton, 2022).

Fig. 7 shows results calculated for crystalline GaAs, for a probe of 200 keV electrons focused onto the beam-entrance surface and incident in the [100] direction. We assume an aberration-free objective lens, so that the diffraction-limited probe diameter Δx , given by Eq. (1), is increased only by combination with the electron-source size. Contours represent electron beam intensity within a 133 nm-thick specimen, with (on the left) the probe centered on a column of Ga atoms and (on the right) the probe focused midway between atomic columns, for three values of the probe-convergence semi-angle α .

In Figs. 7a and 7b, $\alpha=5$ mrad and the probe diameter is 0.3 nm, comparable to the size of the unit cell (lattice parameter 0.56 nm), which contains 8 atoms. Diffraction effects are therefore averaged over several atoms and the exact position of the incident probe makes little

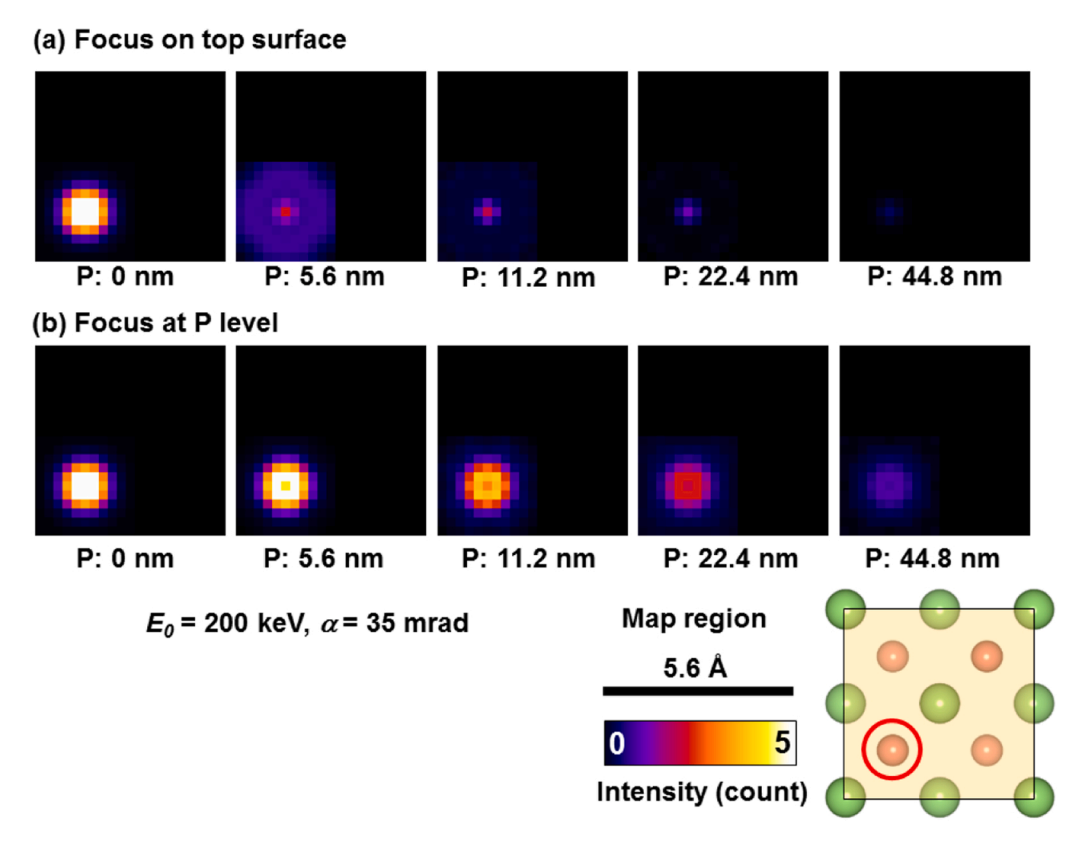


Fig. 9. Simulated phosphorus-K EDX maps for a GaAs crystalline specimen with a single P-atom dopant positioned at different depths below the entrance surface. The probe focal point is (a) on the top (beam-entrance) surface, and (b) at the depth of the atom, as indicated. The simulation was performed for $E_0 = 200 \text{ keV}$ and $\alpha = 35 \text{ mrad}$.

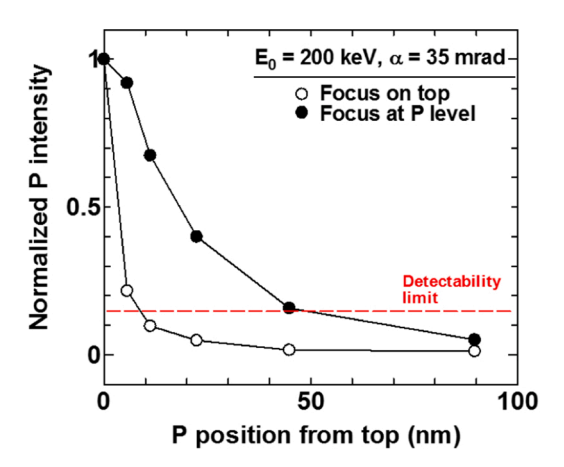


Fig. 10. Phosphorus-K EDX intensities extracted from the maps shown in Fig. 9, plotted against depth of the P atom from the top surface of the GaAs specimen. The dashed line indicates an estimated detection limit.

difference to the electron transmission, which is seen to be relatively unaffected by beam divergence and beam broadening.

In Figs. 7c and 7d, $\alpha=11$ mrad and the probe diameter is 0.14 nm, slightly less than the separation of the Ga and As columns. Incident on an atomic column (Fig. 7c), the beam is strongly focused. But when slightly displaced (Fig. 7d), it is more strongly scattered. Beam divergence occurs below the entrance surface and beam broadening is seen at larger depth.

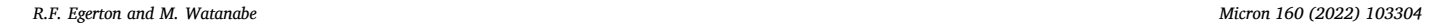
Fig. 7e shows the case of a 0.06 nm probe ($\alpha=25$ mrad) focused onto a Ga column; the electrons are largely channeled towards the exit surface, with limited diffraction. When focused between atomic columns (Fig. 7f), diffraction and beam divergence produce an immediate

spreading, although some electrons are channeled towards the exit surface. So it appears that a small convergent probe focused on the beam-entrance surface might detect *interstitial* atoms located within 4 nm of the surface and perhaps also *substitutional* (dopant) atoms down to a greater depth.

The diameter d_{90} containing 90% of the transmitted electrons is plotted against GaAs thickness in Fig. 8. For $\alpha=2$ mrad, the probe is broadened by diffraction at the objective-lens aperture and not affected appreciably by beam divergence or spreading within the specimen, regardless of probe position. For $\alpha=11$ mrad, d_{90} is initially smaller, but increases rapidly with increasing thickness due to divergence and beamspreading effects, especially for an on-column probe. For $\alpha=25$ or 35 mrad, d_{90} is small at the entrance surface but increases linearly with thickness as a result of the large beam divergence. The overall behavior is therefore similar to that within an amorphous specimen but supplemented by channeling effects that depend on probe size and location.

These focusing properties are relevant to the detection of single-atom dopants in semiconductors by EDX spectroscopic imaging (Watanabe and Egerton, 2022). For example, phosphorus atoms can be substituted for arsenic at As-atom lattice sites. Fig. 9 shows simulated phosphorus maps for single P atoms located at different depths below the top surface of a GaAs crystal. In Fig. 9a, the 200 keV ($\alpha=35~\text{mrad}$) STEM probe is focused on the top (beam-entrance) surface and the multislice simulations suggest that electron channeling might allow a phosphorus atom to remain visible at a depth of several nm (but with much reduced intensity) as a small dot in the phosphorus-K map. The situation is significantly improved if the probe is focused onto the plane containing the P atom, which is now visible down to 22 nm depth with limited image broadening and intensity reduction.

In Fig. 10, the phosphorus-K x-ray intensities extracted from these simulated maps are plotted against P-atom position within the crystal-line GaAs specimen. In this plot, each intensity is normalized to the



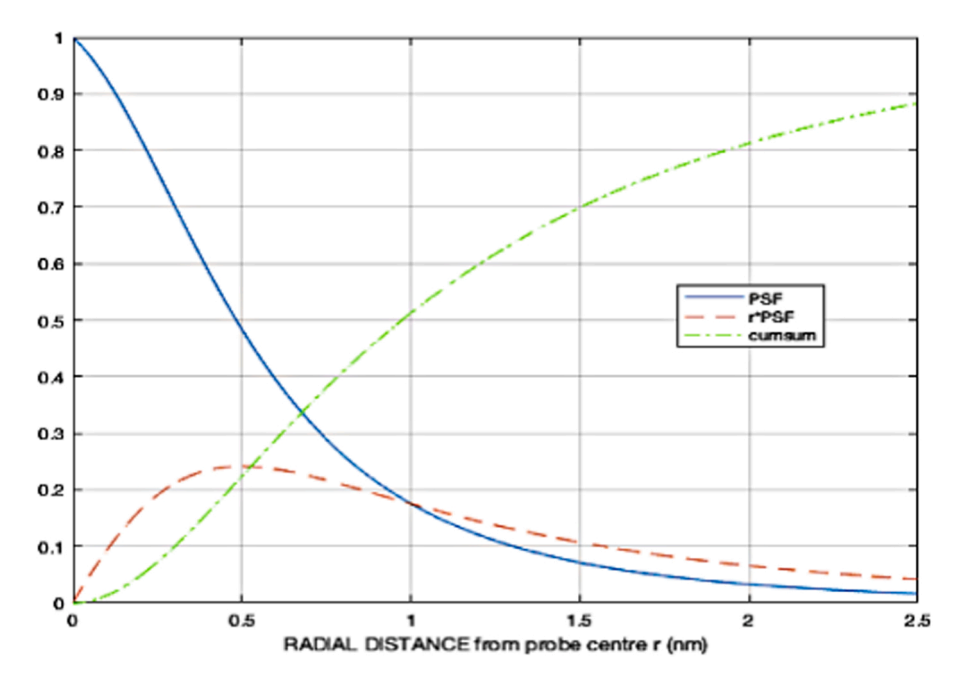


Fig. 11. Continuous blue curve: Coulomb-delocalization PSF for E=25 eV and $E_0=100$ keV. Dashed curve: intensity dI/dr per unit radius. Dash-dot curve: integrated intensity within a given radius r.

value for a P atom on the top surface. The horizontal dashed line indicates the detectability limit, calculated from the P-K and background intensities (see for example: Watanabe et al., 2003; Watanabe and Williams, 2006). The plot suggests that single-atom sensitivity should be possible by adjusting the focal plane of the probe. Thus, isolated dopant and/or impurity atoms in a crystalline specimen might be detectable by through-focal spectroscopy measurements, which would extend and enhance single-atom distribution imaging using the through-focal STE-M-ADF approach (e.g. Voyes, 2006; Wade et al., 2016).

5. Coulomb delocalization

For EELS and some energy-dispersive x-ray (EDX) mapping, spatial resolution may also be limited by a property of inelastic scattering known as Coulomb delocalization.

Elastic scattering involves deflection of a beam electron by the Coulomb field of an atomic nucleus, which (in a neutral atom) terminates on the atomic electrons. To be elastically scattered, an electron must penetrate inside the atom, making the interaction highly localized and allowing the possibility of atomic resolution in elastic images. Inelastic scattering involves Coulomb interaction of a beam electron with atomic electrons, located outside the nucleus. These electrons can be excited from some distance away, making the scattering more delocalized.

A seemingly unrelated view of this delocalization is that it is a consequence of the Heisenberg Uncertainty Principle (HUP): $\Delta p \ \Delta x \sim h$. Angles of inelastic scattering are small, making the transverse momentum Δp small and the uncertainty in lateral coordinate Δx large. A more quantitative version of the Heisenberg principle is the Rayleigh criterion, from which we can derive an approximate formula for the median interaction distance:

$$d_{50} = h/\Delta p = h/(p_0 \theta_{50}) = C/E^{3/4}$$
(22)

where p_0 is the primary-electron momentum and θ_{50} is a median inelastic-scattering angle for electrons whose energy loss (expressed in eV) is E. The coefficient C varies only slowly with primary-electron energy E_0 : its value is known only approximately but plausible values are 17 nm at 200 keV, 15 nm at 100 keV and 11 nm at 30 keV.

As predicted by Eq. (22), the Coulomb delocalization distance has

Table 3 Approximate Coulomb delocalization distances, valid for E0 \approx 60–200 keV.

Energy loss (eV)	FWHM (nm)	d_{50} (nm)	b _{max} (nm)
0.1	0.5	2.5	1000
1	0.2	5	100
10	0.06	1	10
100	0.02	0.15	1

atomic or subatomic dimensions for the large energy losses involved in EDX or core-loss spectroscopy, but is several nm for losses involving valence electrons, and tens of nm for the sub-eV losses associated with dipole modes of atomic vibration. But even for a given energy loss, a single value of the delocalization distance can be misleading. A better way of describing Coulomb delocalization is through its point-spread function, given (Egerton, 2017) by:

$$P_{\rm Cd}(r) \sim (1 + r^2/b_{\rm min}^2)^{-1} \exp(-2r/b_{\rm max})$$
 (23)

where $b_{\rm max} \sim \nu/\omega = \lambda/(2\pi\theta_E)$, $b_{\rm min} \sim \lambda/(4\pi\theta_C)$ and $\theta_E \sim E/(2E_0)$. Eq. (23) assumes a Lorentzian angular distribution of inelastic scattering (with cutoff angle θ_C), valid if the specimen is thin $(t < \lambda_i)$. An example is given in Fig. 11, where $P_{\rm Cd}(r)$ is the continuous curve, representing the intensity per unit area (dI/dA) within the image disk of confusion for electrons of energy loss E. The PSF itself is approximately Lorentzian, with extended tails that contain an appreciable number of inelastically scattered electrons, as seen from the intensity per unit radius dI/dr (dashed curve) and its integral (dash-dot curve).

As illustrated in Table 3, the width (FWHM) of the central peak can be very small but the diameter d_{50} containing half of the electrons is considerably larger and the PSF tails continue up to an even larger diameter, approximately $b_{\rm max} \sim \nu/\omega$. If the noise level in an inelastic image is low enough, the sharp central peak allows characteristic features to be imaged with relatively good resolution (Venkatramen et al., 2018) whereas quantitative analysis may require integration over a more extended distance (such as d_{50}).

FWHM is the width of the central peak of $P_{\rm Cd}(r)$, d_{50} is the median diameter containing 50% of the electrons, and $b_{\rm max}$ is a diameter containing almost all of the electrons. These three quantities are proportional to $E^{1/2}$, $E^{3/4}$ and E^1 respectively (where E= energy loss).

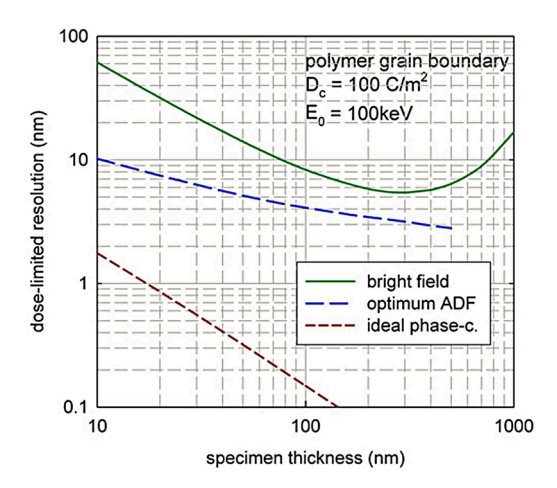


Fig. 12. Calculated dose-limited resolution for 100-keV imaging of a boundary, running throughout the thickness of an organic specimen (characteristic dose 100 C/m^2), where the density changes by 10%. Bright-field TEM solid curve) assumes a 5-mrad objective aperture phase, annular dark field STEM (long-dash curve) is for an optimum inner angle (9 mrad), and TEM phase contrast (short-dash curve) assumes an ideal $\pi/2$ phase plate (Egerton, 2014).

Mapping the optical band gap in insulators involves recording energy losses of just a few eV, so delocalization restricts the spatial resolution to a few nm (Zhan et al., 2017). If Eq. (6) holds, the resolution can be improved by Fourier or Bayesian deconvolution, provided the PSF is known with sufficient accuracy and the noise level in the image is sufficiently low.

Delocalization broadening is independent of specimen thickness but can be reduced by recording electrons scattered through larger angles. For example, an annular detector with an inner semi-angle of $20\theta_{\rm E} \approx 10E/E_0$ would allow a twofold reduction in d_{50} , with a fourfold reduction in inelastic signal. The delocalization diameter d_{50} falls with decreasing primary-electron energy but only by a factor around 1.5 between 200 keV and 30 keV.

6. Electron statistics

Electrons can behave as elementary particles and according to this concept electron scattering consists of random events, governed by Poisson statistics. The probability of a primary electron being inelastically scattered n times is:

$$P_{\rm n} = (1/n!) \, m^{\rm n} \, \exp(-m)$$
 (24)

where $m=t/\lambda_i$ is the mean number of events, t being the specimen thickness and λ_i a mean free path for inelastic scattering. We can regard the number of scattering events as an inelastic signal, whose variance is m and whose standard deviation $m^{1/2}$ represents electronic shot noise. The signal-to-noise ratio is then $\mathrm{SNR}=m^{1/2}$ and can be made large by maximizing the signal, by increasing the beam current or measurement time. But many specimens are beam-sensitive and radiation damage provides a limit. There is therefore an optimum value of m that corresponds to a dose-limited resolution:

DLR ~ (SNR) /
$$[(DQE) F C^2 D_c]^{1/2}$$
 (25)

where SNR is often taken as 3 (Rose criterion), corresponding to $\sim 20\%$ chance of false attribution (Trebbia, 1988).

For good spatial resolution, DLR should be small. This requires an efficient detector (with high detective quantum efficiency DQE), an imaging or spectroscopic procedure having a high efficiency F (the number of signal electrons or photons per incident electron), and a sample that provides a signal that changes by a large fraction between different regions (high contrast C). The remaining factor in Eq. (25) is the *characteristic* dose or fluence D_c : the number of beam electrons (per

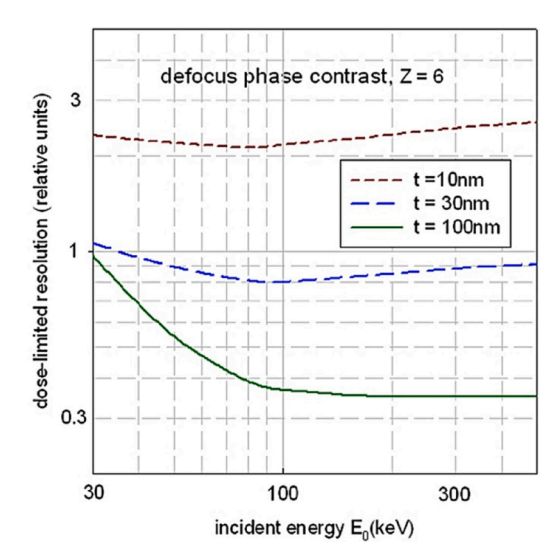


Fig. 13. Calculated dose-limited resolution for phase-contrast imaging of an organic specimen (same conditions as in Fig. 12) with a thickness of 10, 30 or 100 nm, as a function of the TEM accelerating voltage (Egerton, 2014).

unit area of specimen) the sample can withstand before radiation damage destroys the structure being measured.

As specified by Eq. (25), DLR should really be called a damage-limited resolution. But if we replace $D_{\rm c}$ by the actual electron dose D during irradiation, the equation tells us that the spatial resolution starts off poor (high DLR) because of inadequate statistics, reaches an optimum value (for D close to $D_{\rm c}$) and then gets worse because radiation damage is destroying the structure, reducing the contrast C between adjacent regions.

There are two major mechanisms of radiation damage. High-angle elastic scattering can transfer energy (several eV or tens of eV) directly to atomic nuclei, creating knock-on or displacement damage. This process is relatively slow: the cross section σ_e for high-angle scattering is small, making the characteristic fluence large. For an electrically conducting specimen such as a metal, we might have $D_c=1/\sigma_e\approx 10^{11}~e/$ nm², giving DLR $\approx 10^{-3}$ nm. This value lies far below the instrumental and broadening factors discussed above, so radiation damage and electron statistics have negligible effect on the achievable resolution.

In poorly conducting materials, however, the energy transferred to atomic electrons during *inelastic* scattering causes *ionization* damage or *radiolysis*, and also generates secondary electrons that create further radiolysis. For a beam-sensitive specimen such as a polymer, D_c is typically 500 e/nm², giving DLR ≈ 2 nm and this value will likely determine the image resolution.

The DLR formula predicts how different TEM modes compare, for imaging a beam-sensitive specimen. For organic samples, *phase contrast* offers the highest signal efficiency and contrast, and therefore the best resolution, as shown by the brown dashed line in Fig. 12. Therefore cryo-EM of biological specimens nearly always relies on phase contrast. In an *annular dark-field* STEM image, the contrast *C* can be high but the signal efficiency *F* is typically low, making DLR typically worse than for phase contrast, as illustrated by the long-dash blue curve in Fig. 12. *Bright-field* TEM imaging may offer high efficiency but the image contrast is low, especially for very thin specimens, giving a DLR worse than in the other two modes; see the continuous green curve in Fig. 12.

In all imaging modes, the resolution improves as the specimen thickness increases, due to the larger signal (and assuming the object being imaged extends throughout the specimen thickness). But at sufficiently large thickness, plural scattering reduces the signal and/or contrast and the resolution deteriorates.

Eq. (25) also predicts how the accelerating voltage of a TEM affects the dose-limited resolution, shown for phase-contrast imaging in Fig. 13.

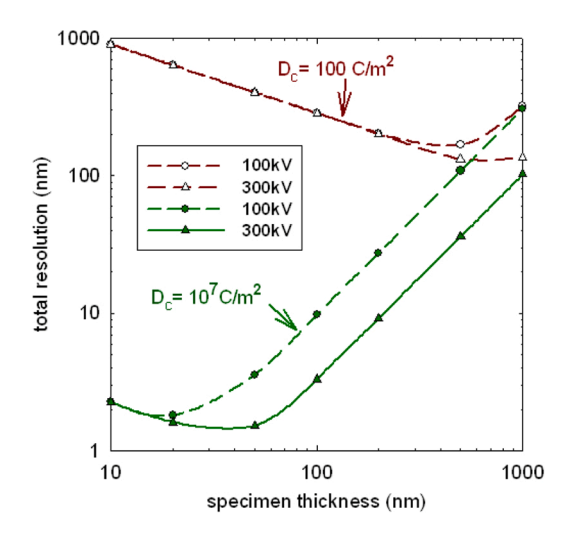


Fig. 14. Calculated resolution for STEM-EDX mapping of 10% iron (using an x-ray detector of DQE = 0.5 and solid angle = 1 sr) in a specimen of density 2 g/cm², for two values of characteristic dose $D_{\rm c}$ and accelerating voltages of 100 kV and 300 kV (Egerton, 2014). The resolution is dose limited for thin specimens but determined by beam spreading for thicker ones.

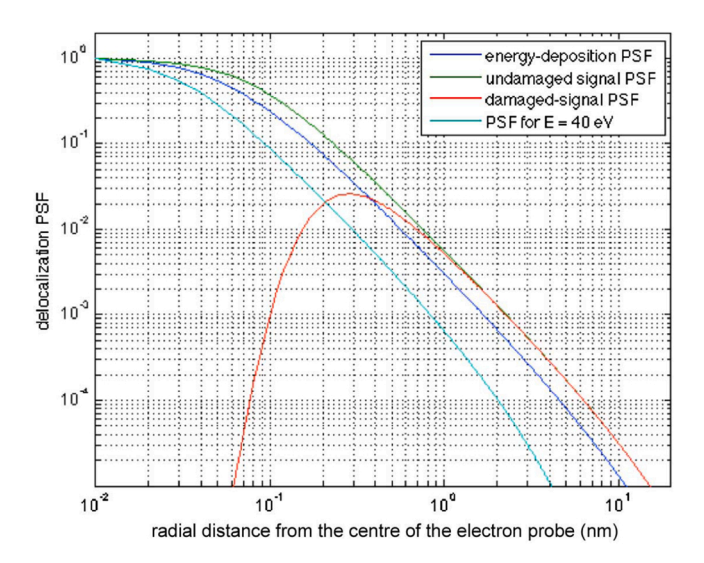


Fig. 15. PSF for energy deposition by 100 keV electrons in a thin specimen of a typical polymer or biological specimen. The dark blue curve is for losses up to 100 eV, the light blue curve includes K-shell losses. Green and red curves show the spatial distribution of an energy-loss signal (E=6 eV) as a function of distance from a sub-Å probe, at the start of irradiation (green) and after considerable damage (red); for details see Egerton (2017).

Assuming equal DQE, an optimized 100 kV TEM might perform as well or better than a 300 kV instrument, for organic specimens that are thinner than 100 nm (Peet et al., 2019).

The DLR values in the previous graphs assume that we image a *single* object, in order to discover its structure. But biologists have long recognized that by assembling molecules (of a protein, for example) into a crystal, the analytical signal can be increased and the damage spread over *many* molecules. More recently, cryo-EM has made use of used *single particle analysis*, where images recorded from many isolated molecules or particles are combined with the help of computer recognition. In addition, the cryo-EM specimen is encapsulated in vitreous ice and cooled to near liquid-nitrogen temperature. This combination of techniques has allowed near-atomic resolution to be obtained from beamsensitive biomolecules.

The idea of dose-limited resolution can be extended to spectroscopic

imaging, such as core-loss energy-filtered imaging or STEM mapping using emitted x-rays. The low core-loss cross sections and low efficiency of x-ray collection result in a poor DLR for a beam-sensitive specimen, illustrated in Fig. 14 by the brown curve at the top. The green curve is for a less sensitive material, where the analytical resolution might be of the order of 1 nm for thin sample but becomes worse at higher thickness because of beam spreading.

6.1. PSF for radiolysis

Because radiolysis results from *delocalized* inelastic scattering, its spatial extent can be represented by a point-spread function. It is common to assume that the degree of radiolytic damage is proportional to the energy deposited per unit volume (or mass) of specimen, the basis of the Gray unit of dose (Egerton, 2021). By summing the Coulomb-delocalization PSF over all values of energy loss, we can calculate a PSF for energy deposition that relates directly to radiolysis damage. The dark-blue curve in Fig. 15 shows this PSF for 100 keV electrons passing through a thin organic specimen, taking energy losses up to 100 eV. However, allowance should be made for the K-shell excitation, which represents only about 1% of the inelastic scattering but nearly one quarter of the energy deposition. The light-blue curve is an estimate of the PSF for all energy losses, taking a mean energy loss of $E_{\rm av} = 40$ eV in Eq. (22).

Energy deposition is highest at the *center* of a small probe (impact parameter b=0), so damage starts there and spreads outwards. If we record EELS data representing *undamaged* material, this signal will disappear at small radial distances, leaving only signal that is generated by *delocalized* interaction of the probe with its immediate surroundings, represented by the red curve in Fig. 15.

The inelastic scattering of primary electrons is not the only source of radiolytic damage. Secondary electrons (generated by inelastic scattering) travel through the specimen, undergoing inelastic collisions and creating their own damage. Fast secondaries (FSE, with starting energy greater than 50 eV) can travel a few nm beyond a focused probe, adding to the energy deposition at larger radial distance. A simple calculation, based on the energy-loss spectrum of a typical organic material, suggests that the fraction of FSE energy deposited outside a radius r is roughly 0.7 nm/r (Egerton and Malac, 2004). The PSF for fast-secondary damage has a r^3 tail, in broad agreement with Monte Carlo calculations (Joy, 1983)

Since electrons cannot be focused to a point, these point-spread functions must be broadened to allow for the probe diameter. The current density distribution within a small (diffraction-limited) probe approximates to a Gaussian function and this non-uniform current-density distribution also implies faster damage at the center of the probe, in addition to the effects of delocalization and secondary electrons. STEM imaging involves additional variables such as scanning rate and scan pattern (raster or non-raster) that have been found to affect the information/damage ratio. Understanding the role of these parameters could help to optimize the resolution of STEM images recorded from beam-sensitive specimens (Velazco et al., 2022).

Coulomb delocalization can be exploited to reduce radiolysis damage, by using an aloof STEM probe positioned at a distance b beyond the edge of a specimen. For an EELS signal corresponding to an energy loss of a few eV or less, the damage can be lower by several orders of magnitude, especially for larger b (Egerton, 2015; Rez et al., 2016). The median resolution is approximately ($b_{\text{max}}b^{1/2}$ for volume losses (Egerton, 2018), so as usual there is a trade-off between resolution and damage. Leapfrog scanning (scan step > delocalization distance) is another attempt to exploit Coulomb delocalization and can (according to simulations) extract more energy-loss signal from a beam-sensitive sample, for a given spatial resolution (Egerton, 2019).

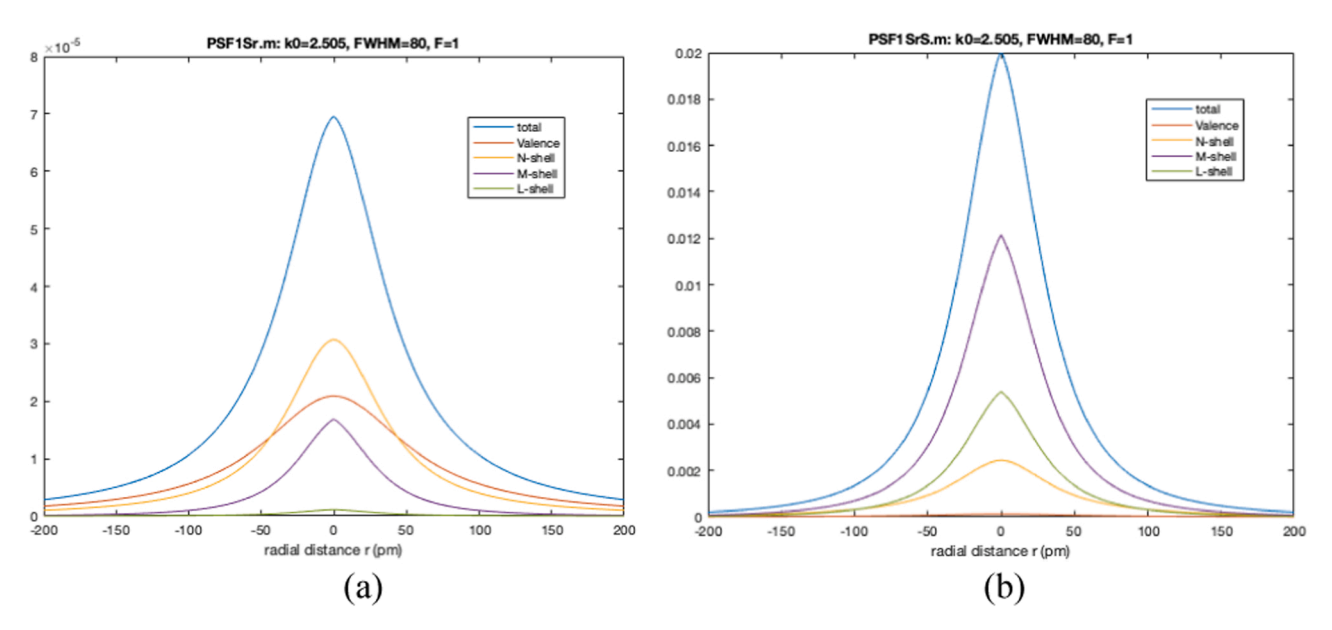


Fig. 16. (a) Point-spread functions for SE generation from different atomic shells of a strontium atom, weighted according to the cross section of each shell and appropriate to an *adatom on a surface*. (b) Point-spread functions for SE generation from atomic shells of a strontium atom *within in a matrix*, weighted proportional to the stopping power of each shell.

7. Spatial resolution of secondary-electron images

The scanning electron microscope (SEM) makes use of secondary electrons (SE) emitted from within the escape depth of a thick (bulk) specimen. The SE provide an image that provides topographical contrast, with a resolution of the order of the escape depth: typically about 1 nm in metals but up to several nanometers in insulating specimens (Reimer, 1998). Backscattered electrons (BSE) emerge from deeper regions (up to half the electron range) and generate a signal that gives material or atomic-number contrast, although with lower resolution except at low primary energies where the electron range is small. BSE generate additional secondary electrons (SE2) that add extended tails to the secondary-electron PSF and reduce the contrast of the SE image.

Adding a SE detector to a STEM provides SE images with resolution sometimes below 1 nm, with negligible contribution from SE2 electrons because of the thin specimen (Liu and Cowley, 1988; Howie, 1995). With an aberration-corrected objective lens and a 200 keV field-emission source, a probe size below 0.1 nm can be achieved, resulting in the first atomic-scale SE images of heavy atoms on a thin carbon support (Zhu et al., 2009). Although surprising at the time, atomic resolution can be explained in terms of the PSF for SE generation, whose FWHM has subatomic dimensions (Inada et al., 2011). SE images of thin crystalline specimens displayed the atomic lattice and a detailed treatment of the image contrast was eventually developed (Brown et al., 2013).

Point-spread functions for SE generation can be calculated from Eq. (23). In heavy atoms, many of the secondary electrons are generated from *inner* atomic shells; see Fig. 16a. In fact, these shells contribute most of the stopping power and generate energetic SE that can create further secondaries if the atom is surrounded by other atoms within the SE escape depth; see Fig. 16b. As seen in both of these Figures, the PSFs have subatomic widths, which accounts for the visibility of both adatoms and atomic columns in SE images (Egerton and Zhu, 2022).

8. Summary and conclusions

The spatial resolution of a TEM or STEM depends on the performance of the instrument (including its electron optics) and on the imaging mode (bright field, dark field, phase or amplitude contrast, *etc.*). Spatial

resolution also depends on the specimen, particularly its thickness and radiation sensitivity. Rather than a single number, the resolution is better represented by a point-spread function, which predicts both resolution and image contrast. We have given equations for the major optics- and specimen-related resolution factors, including point-spread functions.

Electron-optical limits to resolution are improved by correcting objective-lens spherical aberration and (for low kV) chromatic aberration. Beam broadening is reduced by using a very thin specimen or (for bright-field images) by using an angle-limiting collection aperture. Coulomb delocalization in inelastic images is reduced by collecting higher-angle scattering, at the expense of reduced signal and degraded dose-limited resolution. Multimodal microscopy (collecting several signals: EELS, HAADF etc.) from the same specimen increases the information available and with the use of an optimization algorithm can increase the signal/noise ratio and spatial resolution (Schwartz et al., 2022).

Fundamental limits to resolution arise from both the wave and particle properties of electrons. Ptychography seeks to overcome the Rayleigh wavelength limit by oversampling the specimen with a defocused STEM probe, recording a far-field diffraction pattern using a fast two-dimensional detector, and using a reconstruction algorithm to deduce the structure. The term 4D-STEM is sometimes used to denote the two dimensions of real *and* reciprocal space (Ophus, 2019). Ptychography is capable of three-dimensional imaging (Gao et al., 2017) and has been applied to practical problems, including cryo-EM (Pelz et al., 2017) and Li-battery materials (Lozano et al., 2018). Recognizing the partial-coherence properties of the probe, Chen et al. (2020) report a mixed-state ptychographic approach that may offer subatomic resolution, or a substantial reduction in electron dose for the same resolution.

Deconvolution techniques can improve the resolution of a TEM or STEM image but are limited by the shot noise arising from the particle nature of electrons. Quantum electron microscopy (QEM) attempts to deal with this aspect. One option is to make each electron pass multiple times through a thin specimen, increasing the information without increasing the shot noise (Juffmann et al., 2017). Other ideas include the use interferometry to achieve interaction-free microscopy (Turner et al., 2021) and joint measurement of the transmitted electron and a collective mode of sample excitation (Rotunno et al., 2021). All of these projects are challenging in terms of instrumentation, but successful

implementation might increase the spatial resolution of phase-contrast cryo-EM by a factor of 3 - 4 (Koppell et al., 2022).

Declaration of Competing Interest

The authors declare that they have no known competing financial interests or personal relationships that could have appeared to influence the work reported in this paper.

Acknowledgments

RFE thanks the Natural Sciences and Engineering Research Council of Canada (NSERC) for continuing support, and the organizers of an online JSM/MSC meeting (November 2021) for the opportunity to present ideas contained in this review. M.W. wishes to acknowledge financial support from the National Science Foundation through grants DMR-2018683 and CMMI-2016279.

References

- Batson, P.E., 2009. Control of parasitic aberrations in multipole optics. J. Electron Microscopy 58, 123–130.
- Bothe, W., 1951. Die Streuung von Elektronen in schrägen Folien. Sitzungsb. Heidelber. Akad. Wiss. 7, 307–316.
- Brown, H.G., D'Alfonso, A.J., Allen, L.J., 2013. Secondary electron imaging at atomic resolution using a focused coherent electron probe. Phys. Rev. B 87, 054102.
- Chen, Z., Odstrcil, M., Jiang, Y., Han, Y., Chiu, M.-H., Li, L.-J., Muller, D.A., 2020. Mixed-state electron ptychography enables sub-angstrom resolution imaging with picometer precision at low dose. Nat. Commun. 11, 2994.
- Cliff, G. & Lorimer, G.W., 1981. Influence of plural electron scattering on x-ray spatial resolution in TEM thin foil microanalysis. In: Quantitative Microanalysis with High Spatial Resolution (ed. by G. W. Lorimer. M. H. Jacobs and P. Doig), pp. 47–52. Metals Society, Manchester.
- Crewe, A.V., Wall, J., Langmore, J., 1970. Visibility of a single atom. Science 168, 1338–1340.
- Demers, H., Ramachandra, R., Drouin, D., de Jonge, N., 2012. The probe profile and lateral resolution of scanning transmission electron microscopy of thick specimens. Microsc. Microanal. 18, 582–590.
- Drees, H., Müller, E., Dries, M., Gerthsen, D., 2018. Electron-beam broadening in amorphous carbon films in low-energy scanning transmission electron microscopy. Ultramicroscopy 185, 65–71.
- Egerton, R.F., 2014. Choice of operating voltage for a transmission electron microscope. Ultramicroscopy 145, 85–93.
- Egerton, R.F., 2015. Vibrational-loss EELS and the avoidance of radiation damage. Ultramicroscopy 159 (2015), 95–100.
- Egerton, R.F., 2017. Scattering delocalization and radiation damage in STEM-EELS. Ultramicroscopy 180, 115–124.
- Egerton, R.F., 2018. The spatial resolution of aloof EELS. www/tem-eels.ca/educational materials/AloofSpatRes.pdf.
- Egerton, R.F., 2019. Radiation damage to organic and inorganic specimens in the TEM. Micron 119, 72–87.
- Egerton, R.F., 2021. Dose measurement in the TEM and STEM. Ultramicroscopy 229, 113363.
- Egerton, R.F., Crozier, P.A., 1997. The effect of lens aberrations on the resolution of an energy-filtered TEM. Micron 28, 117–124.
- Egerton, R.F., Malac, M., 2004. The lateral range and energy deposition of fast secondary electrons. Microsc. Microanal. 10 (suppl. 2), 1382–1383.
- Egerton, R.F., Zhu, Y., 2022. Spatial resolution in secondary-electron microscopy. Microscopy (Special Issue on Frontiers of Resolution in Microscopy), in press.
- Elbaum, M., Seifer, S., Houben, L., Wolf, S.G., Rez, P., 2021. Toward compositional contrast by cryo-STEM. Acc. Chem. Res. https://doi.org/10.1021/acs. accounts.1c00279.
- Gao, S., Peng Wang, P., Fucai Zhang, F., Martinez, G.T., Nellist, P.D., Pan, X., Kirkland, A. I., 2017. Electron ptychographic microscopy for three-dimensional imaging. Nat. Commun. 8, 163. https://doi.org/10.1038/s41467-017-00150-1.
- Gauvin, R., Rudinsky, S., 2016. A universal equation for computing the beam broadening of incident electrons in thin films. Ultramicroscoipy 167, 21–30.
- Geiss, R.H., Kyser, D.F., 1979. Thin film x-ray spectrometry. Ultramicroscopy 3, 379-400.
- Gentsch, P., Gilde, H., Reimer, L., 1974. Measurement of the top-bottom effect in STEM of thick amorphous specimens. J. Microsc. 100, 81–92.
- Goldstein, J.I.Costley, Lorimer, G.W., Reed, S.F.B., 1977. Quantitative x-ray analysis in the electron microscope. In: Johari, O. (Ed.), Scanning Electron Microscopy. SEM Inc. (IITRI), Chicago, pp. 315–324.
- Groves, T., 1975. Thick specimens in the CEM and STEM: resolution and image formation. Ultramicroscopy 1, 170–172, 115-31.
 Haider, M., Müller, H., Uhlemann, S., Zach, J., Loebau, U., Hoeschen, R., 2008.
- Haider, M., Müller, H., Uhlemann, S., Zach, J., Loebau, U., Hoeschen, R., 2008. Prerequisites for a C_c/C_s-corrected ultrahigh-resolution TEM. Ultramicroscopy. 108, 167–178.

- Hovington, P., Drouin, D., Gauvin, R., 1997. CASINO: a new Monte Carlo code in C language for electron beam interaction. Scanning 19 (1–14), 20–28.
- Howie, H., 1995. Recent developments in secondary electron imaging. J. Microsc. 180, 192–203.
- Hyun, J.K., Ercius, P., Muller, D.A., 2008. Beam spreading and spatial resolution in thick organic specimens. Ultramicroscopy 109, 1–7.
- Inada, H., Su, D., Egerton, R.F., Konno, M., Wu, L., Ciston, J., Wall, J., Zhu, Y., 2011. Atomic imaging using secondary electrons in a scanning transmission electron microscope: experimental observations and possible mechanisms. Ultramicroscopy 111, 865–876.
- Ishizuka, K., 2012. Prospects of atomic resolution imaging with an aberration-corrected STEM. J. Electron Microsc. 50, 291–305.
- de Jonge, N., Verch, A., Demers, H., 2018. The influence of beam broadening on the spatial resolution of annular dark field scanning transmission electron microscopy. Microsc. Microanal. 24, 8–16.
- Joy, D.C., 1983. The spatial resolution limit of electron lithography. Microelectron. Eng. $1,\,103-119$.
- Joy, D.C., 1995. Monte Carlo Modeling for Electron Microscopy and Microanalysis. Oxford Series in Optical and Imaging Sciences, OUP.
- Juffmann, T., Koppell, S.A., Klopfer, B.B., Ophus, C., Glaeser, R., Kasevich, M., 2017.
 Multi-pass transmission electron microscopy. Sci. Rep. 7, 1699.
- Kirkland, E.J., 2020. Advanced Computing in Electron Microscopy, 3rd edition. Springer Nature, Switzerland.
- Koppell, S.A., Israel, Y., Bowman, A.J., Klopfer, B.B., Kasevich, M.A., 2022. Transmission electron microscopy at the quantum limit. arXiv:2201.09183v1 [physics.app-ph] 23 Jan 2022
- Kyser, D.F., 1979. Introduction to Analytical Electron Microscopy, ed. J.J. Hren, J.I. Goldstein and D.C. Joy, (Plenum, New York), 199–221.
- Lee, S.B., Han, H.N., 2021. Faceting-roughening transition of a Cu grain boundary under electron-beam irradiation at 300 keV. Sci. Rep. 11, 15563 (9 pages) doi.org/ 10.1038/s41598-021-95091-7.
- Liu, J., Cowley, J.M., 1988. Contrast and resolution of secondary electron images in a scanning transmission electron microscope. Scan. Microsc. 2, 1957–1970.
- Lozano, J.G., Martinez, G.T., Jin, L., Nellist, P.D., Bruce, P.G., 2018. Low-dose aberration-free imaging of Li-rich cathode materials at various states of charge using electron ptychography. Nano Lett. 18, 6850–6855.
- Mandelbrot, B.B., 1982. The Fractal Geometry of Nature. W.H. Freeman and Company, New York.
- Michael, J.R., Williams, D.B., 1987. A con sistent definition of probe size and spatial resolution in the analytical electron microscope. J. Microsc. 147, 289–303.
- Muller, D.A., Grazul, J., 2001. Optimizing the environment for sub-0.2 nm scanning transmission electron microscopy. J. Electron Microsc. 50, 219–226.
- Nellist, P.D., Behan, G., Kirkland, A.J., Hetherington, C.J.D., 2006. Confocal operation of a transmission electron microscope with two aberration correctors. Appl. Phys. Lett. 89, 124105.
- Newbury, D.E., Myklebust, R.L., 1979. Monte Carlo electron trajectory simulation of beam spreading in thin foil targets. Ultramicroscopy 3, 391–395.
- Ophus, C., 2019. Four-dimensional scanning transmission electron microscopy (4D-STEM): from scanning nanodiffraction to ptychography and beyond. Microsc. Microanal. 25, 563–582.
- Peet, M.J., Henderson, R., Russo, C., 2019. The energy dependence of contrast and damage in electron cryomicroscopy of biological molecules. The energy dependence of contrast and damage in electron cryomicroscopy of biological molecules. Ultramicroscopy 203, 125–131.
- Pelz, P.M., Qiu, W.X., Bücker, R., Kassier, G., Miller, R.J.D., 2017. Low-dose cryo electron ptychography via non-convex Bayesian optimization. Sci. Rep. 7, 9883.
- Reimer, L., 1998. Scanning Electron Microscopy: Physics of Image Formation and Microanalysis, 2nd edition. Springer, Berlin.
- Reimer, L., Kohl, H., 2008. Transmission Electron Microscopy, 5th edition (Springer, New York), p. 188–192.
- Rez, P., 1983. A transport equation theory of beam spreading in the electron microscope. Ultramicroscopy 12, 29–38.
- Rez, P., Larsen, T., Elbaum, M., 2016. Exploring the theoretical basis and limitations of cryo-STEM tomography for thick biological specimens. J. Struct. Biol. 196, 456–478.
- Rez, R. Aoki, T., March, K., Gur, D., Krivanek, O.L., Dellby, N., Lovejoy, T.C., Wolf, S.G., & Hagai Cohen, H, 2016. Damage-free vibrational spectroscopy of biological
- materials in the electron microscope. Nature Communications 7, 10945 (7 pages). Rose, H., 1975. The influence of plural scattering on the limit of resolution in electron microscopy. Ultramicroscopy 1, 167–169.
- Rotunno, E., Gargiulo, S., Vanacore, G.M., Mechel, C., Tavabi, A.H., Dunin-Borkowski, R. E., Carbone F., Maidan, I., Zanfrognini, M., Frabboni, S., Guner, T., Karimi, E., Kaminer, I., Grillo, V., 2021. One-dimensional ghost imaging with an electron microscope: a route towards ghost imaging with inelastically scattered electrons. https://arxiv.org/pdf/2106.08955.pdf.
- Schwartz, J., Di, Z.W., Jiang, Y., Fielitz, A.J., Ha, D.-H., Perera, S.D., Baggari, I.E., Robinson, R.D., Fessler, J.A., Ophus, C., Rozeveld, S., Hovden, R., 2022. Imaging atomic-scale chemistry from fused multi-modal electron microscopy. Computational Materials 16, 1–6. (www.nature.com/npjcompumats).
- Sousa, A.A., Hohmann-Marriott, M.F., Zhang, G., Leapman, R.D., 2009. Monte Carlo electron-trajectory simulations in bright-field and dark-field STEM: Implications for tomography of thick biological sections. Ultramicroscopy 109, 213–221.
- Spence, J.C.H., 2013. High-Resolution Electron Microscopy, 4th Edition. Oxford University Press.
- Trebbia, P., 1988. Unbiased method for signal estimation in electron energy loss spectroscopy, concentration measurements and detection limits in quantitative microanaysis: methods and programs. Ultramicroscopy 24, 399–408.

- Turner, A.E., Johnson, C.W., Kruit, P., McMorran, B.J., 2021. Interaction-free measurement with electrons. Phys. Rev. Lett. 127, 110401.
- Turner, J.H., O'Keefe, M.A., Mueller, R., 1997. Design and implementation of a site for a one-Angstrom TEM. Proc. Microsc. Microanal. 3, 1177–1178.
- Van Cappellan, E., Schmitz, A., 1992. A simple spot-size versus pixel-size criterion for x-ray microanalysis of thin foils. Ultramicroscopy 41, 193–199.
- Velazco, A., Béché, A., Jannis, D., Verbeeck, J., 2022. Reducing electron beam damage through alternative STEM scanning strategies, Part I: Experimental findings Ultramcroscopy 232, 113398. https://doi.org/10.1016/j.ultramic.2021.113398.
- Venkatramen, Kartik, Rez, Peter, March, Katia, Crozier, Peter, 2018. The influence of surfaces and interfaces on high spatial resolution vibrational EELS from SiO₂. Microscopy i14–i18. https://doi.org/10.1093/jmicro/dfy003.
- Voyes, P.M., 2006. Imaging single atoms with Z-contrast STEM in two and three dimensions. Microchem. Acta 155, 5–10.
- Wade, C.A., McLean, M.J., Vinci, R.P., Watanabe, M., 2016. Aberration-corrected scanning transmission electron microscope (STEM) through-focus imaging for threedimensional atomic analysis of bismuth segregation in copper [001]/33deg.-twist bicrystal grain boundaries. Microsc. Microanal. 22, 679–689.
- Wan, W., Chen, F.-R., Zhu, Y., 2018. Design of compact ultrafast microscopes for singleand multi-shot imaging with MeV electrons. Ultramicroscopy 198, 143–153.

- Warner, J., Margine, E.R., Mukari, M., Robertson, A.W., Giustino, F., Kirkland, A.I., 2012. Dislocation-driven deformations in graphene. Science 337, 209–212.
- Watanabe, M., Egerton, R.F., 2022. Evolution in x-ray analysis from micro to atomic scales in aberration-corrected scanning transmission electron microscopes. Microscopy 71 (suppl. 1), i32–i47. https://doi.org/10.1093/jmicro/dfab026.
- Watanabe, M., Williams, D.B., 2006. The quantitative analysis of thin specimens: a review of progress from the Cliff-Lorimer to the new ζ-Factor methods. J. Microsc. 221, 89–109.
- Watanabe, M., Williams, D.B., Tomokiyo, Y., 2003. Comparison of detectability limits for elemental mapping by EF-TEM and STEM-XEDS. Micron 34, 173–183.
- Wolf, S.G., Shimoni, E., Elbaum, M., Houben, L., 2018. STEM tomography in biology. In: Cellular Imaging, ed. E. Hanssen (Springer International Publishing) https://doi.org/ 10.1007/978-3-319-68997-5_2.
- Zaluzec, N.J., 2003. The scanning confocal electron microscope. Microscopy Today 2003. 8–12.
- Zhan, W., Granerød, C.S., Venkatachalapathy, V., Johansen, K.M.H., Jensen, I.J.T., Kuznetsov, A., Yu, Prytz, Ø., 2017. Nanoscale mapping of optical band gaps using monochromated electron energy loss spectroscopy. Nanotechnology 28 (105703), 6.
- Zhu, Y., Inada, H., Nakamura, K., Wall, J., 2009. Imaging single atoms using secondary electrons with an aberration-corrected electron microscope. Nat. Mater. 8, 808–812.